ACS APPLIED MATERIALS & INTERFACES

Article

Plasmonic Effect of Gold Nanostars in Highly Efficient Organic and Perovskite Solar Cells

Riski Titian Ginting, Sandeep Kaur, Dong-Kwon Lim, Jung-Mu Kim, Joong-Hee Lee, Seung Hee Lee, and Jae-wook Kang

ACS Appl. Mater. Interfaces, **Just Accepted Manuscript** • DOI: 10.1021/acsami.7b11084 • Publication Date (Web): 22 Sep 2017

ACS Publications

ACS Applied Materials & Interfaces is published by the American Chemical Society.
1155 Sixteenth Street N.W., Washington, DC 20036

Plasmonic Effect of Gold Nanostars in Highly Efficient Organic and Perovskite Solar Cells

Riski Titian Ginting,[a,1] *Sandeep Kaur,*[b,1] *Dong-Kwon Lim,*[c] *Jung-Mu Kim,*[d] *Joong Hee Lee,*[b] *Seung Hee Lee,*[*,b] and *Jae-Wook Kang*[*,a]

[a] Department of Flexible and Printable Electronics, Polymer Materials Fusion Research Center, Chonbuk National University, Jeonju 54896, Republic of Korea

[b] Applied Materials Institute for BIN Convergence, Department of BIN Convergence Technology and Department of Polymer-Nano Science and Technology, Chonbuk National University, Jeonju 54896, Republic of Korea

[c] KU-KIST Graduate School of Converging Science and Technology, Korea University, Seoul 136-701, Republic of Korea

[d] Department of Electronic Engineering, Chonbuk National University, Jeonju 54896, Republic of Korea

[1] R.T. Ginting, and S. Kaur made equal contribution to this paper

*To whom correspondence should be addressed.

Prof. Sung Hee Lee (E-mail: lsh1@chonbuk.ac.kr)

Prof. Jae-Wook Kang (E-mail: jwkang@jbnu.ac.kr)

Keywords: gold nanostar, plasmonic, organic solar cells, perovskite solar cells, near-field enhancement, backscattering, impedance

Abstract

Herein, a novel strategy is presented for enhancing light absorption by incorporating gold nanostars (Au NSs) into both the active layer of organic solar cells (OSCs) and the rear-contact hole transport layer (HTL) of perovskite solar cells (PSCs). We demonstrate that the power conversion efficiencies of OSCs and PSCs with embedded Au NSs are improved by 6% and 14%, respectively. We find that pegylated Au NSs are greatly dispersable in chlorobenzene solvent, which enabled complete blending of Au NSs with the active layer. The plasmonic contributions and accelerated charge transfer are believed to improve the short-circuit current density and fill factor. This study demonstrates the roles of plasmonic nanoparticles in the improved optical absorption, where the improvement in OSCs was attributed to surface plasmon resonance (SPR) and in PSCs was attributed to both SPR and the backscattering effect. Additionally, devices including Au NSs exhibited better charge separation/transfer, reduced charge recombination rate, and efficient charge transport. This work provides a comprehensive understanding of the roles of plasmonic Au NS particles in OSCs and PSCs, including an insightful approach for the further development of high-performance optoelectronic devices.

Introduction

For the past few years, extensive efforts have been devoted to boost the photovoltaic performance of organic solar cells (OSCs) and perovskite solar cells (PSCs), owing to their cost-effectiveness, ease of fabrication, light weight, and potential as mainstream energy harvesting sources. Despite the high efficiency of OSCs[1] and PSCs,[2] their poor optical absorption efficiency and inefficient charge transport represent major obstacles to improving their power conversion efficiency (PCE). Different strategies have been explored in the past to improve the optical absorption capability in OSCs and PSCs, including the use of surface texturing,[3] micro-lenses,[4] nanograting,[5] and photonic crystals[6-7] to increase light trapping efficiency. Among these, one prominent approach is to utilize plasmonic metal nanoparticles (NPs) to improve the photovoltaic performance of OSCs and PSCs through plasmon optical and electrical effects. The optical effects include plasmon-enhanced scattering, propagation of surface plasmon polariton modes, and excitation of localized surface plasmon resonance (LSPR), and the electrical effects include hot carrier generation, efficient charge transport, and efficient carrier extraction.[8-9] Utilizing the localized surface plasmonic effect of metal NPs, which arises from the collective oscillations of conduction electrons of metal and incident electromagnetic waves, allows strengthening of the light harvesting by increasing the absorption and scattering of incident light. Surface plasmons associated with metal NPs enhance the localized field due to the scattering of light and increasing the optical path length, which aids light propagation in the active layer and increases exciton generation. In addition, metal NPs exhibit strong absorption in the UV–visible range, which is within the optical absorption region of the organic and perovskite layers used in OSCs and PSCs. Therefore, by changing the geometrical parameters of metal NPs such as size,

shape, or dielectric environment, their optical properties can be easily tuned[10-11] to enhance the overall photovoltaic performance.

Various research groups have reported enhancements in the PCE of OSCs through the use of various nanostructures and metal NP sizes, especially using Au[12-13] and Ag,[14] after blending in the active layer,[12, 15] anode buffer layer,[14, 16-17] or at the interface.[18-19] Amid the plethora of reports on using metal NPs to enhance efficiency, ensuring uniform dispersion of these NPs while maintaining the surface morphology in the active layer and the electron transport layer (ETL) or hole transport layer (HTL) has always remained a critical concern. It has been reported that the incorporation of metal plasmonic nanostructures in the front side layer (in mesoporous and thin film configurations) of PSCs such as TiO_2,[20-22] NiO,[23] and PEDOT:PSS[24] leads to promising enhancements of photovoltaic performance. Previously, penetrated gold metal evaporated into [6,6]-phenyl-C_{61}-butyric acid methyl ester was found to be advantageous in changing the optical density due to plasmonic effects;[25] therefore, these findings demonstrate opportunities for new designs incorporating plasmonic nanostructures in the rear contacts of PSCs. Incorporating Au NPs into poly(3-hexylthiophene-2,5-diyl) (P3HT) as the rear HTL of PSCs has led to significant improvement in photovoltaic performance, owing to light scattering induced by the additional photon absorption of the perovskite layer.[26] However, the PCEs yielded by this approach are relatively low compared to those of the commonly used 2,2′,7,7′-tetrakis[N,N-di(4-methoxyphenyl)amino]-9,9′-spirobifluorene (spiro-OMeTAD) HTL. So far, only slight improvements to the PCE have been realized when embedding the Au NPs in spiro-OMeTAD due to the non-uniform distribution of the Au nanoparticles (Au NPs) used.[27] In contrast, the insertion of gold nanorods (Au NRs) into a TiO_2 layer at the rear side of OSCs has

yielded 13% improvement to power conversion efficiency (PCE) due to backscattering and localized SPR.[28]

In this study, Au NSs were employed as the metal plasmonic nanostructures because their anisotropic morphologies (namely, a central core with several extending round-edged tip branched nanostructures) yield strong local electromagnetic field enhancements compared to those of other gold nanostructures[29-30] and because they have great potential in improving light absorption in the active layer.[31] Au NSs embedded into the buffer layer of OSCs exhibit significant enhancement in PCE,[31] but so far the plasmonic effect of Au NSs in active layer of OSCs and the use of Au NSs acting as rear contact scatterers in PSCs have not been investigated, making this is a highly desirable area of study. Herein, we demonstrate the successful embedment of highly dispersed (methoxypolyethylene glycol thiol) mPEG thiol–modified gold nanostars (mPEG-Au NSs) into blended layers of thieno[3,4-*b*]thiophene/benzodithiophene (PTB7):[6,6]-phenyl-C_{71}-butyric acid methyl ester ($PC_{71}BM$; hereinafter PCBM) and the perovskite/spiro-OMeTAD interface, resulting in 6 and 14% PCE improvements, respectively. The mPEG-thiol was used as capping agent in order to improve the dispersion and stability of the Au NS particles in chlorobenzene solution. The present work includes a systematic investigation of the morphologies of Au NSs, the photovoltaic performances, and the optical and electrical contributions of Au NSs in these cells. This work also includes optical simulations performed to further understand the underlying mechanism of the improvement in device performance after the incorporation of Au NSs.

Results and discussion

Figures 1a and 1b depict the typical inverted-type OSC and conventional-type PSC device configurations that were used in this study. The Au NSs incorporated in the active layers of OSCs and the HTLs of PSCs were synthesized by means of reducing chloroauric acid ($HAuCl_4$) in the presence of a hydroxylamine hydrochloride (NH_2OH-HCl) reducing agent and phosphate buffer. Details on the synthetic procedure are given in the *Experimental Details* section. The morphology of Au NSs was characterized by means of transmission electron microscopy (TEM), which showed that they were distributed uniformly and well controlled with sizes around 35 nm; the formation of multiple spikes was also clearly evident, showing that the particles were Au NSs (Figure 1c). In detail, the average size distribution of the Au NS diameter, core size of the Au NSs, and spike length are plotted in Figures S1a-c, where the core to spike ratio is 2.6. Surface plasmonic absorption spectra of the prepared Au NSs dispersion acquired before and after mPEG-thiol modification are shown in Figure 1d. The mPEG-Au NSs exhibited a pronounced surface plasmonic resonance peak at 630 nm in chlorobenzene (CB) solution, which is red shifted by 10 nm compared to that without mPEG-thiol because of the change in dielectric medium of Au NSs.[32] Based on Figures S2a and S2b, Au NSs were successfully incorporated within the active layer of OSCs and at the perovskite/HTL interface of PSCs, due to the highly dispersed Au NSs in the CB solution.

The performance of the PSCs prepared without (as a control) and with Au NSs was systematically characterized to investigate the effectiveness of the plasmonic particles in improving the solar cell performance. Figure 2a shows the current density–voltage (*J–V*) characteristics of a control and OSC embedded with Au NSs device. As summarized in Table 1, incorporation of Au NSs into the active layer yielded slight improvements in the V_{oc}, J_{sc}, and FF compared to the control device, leading to enhancement of PCE from 8.30 to 8.78%. The

optimum concentration of Au NSs was achieved at 0.01 wt%, above which the photovoltaic performance began to decrease (Figure S3). As comparison, gold nanoparticles (Au NPs) of size 20–30 nm were also embedded in the active layer and the resulting photovoltaic parameters were evaluated (Figs. S4a,b). These Au NPs yielded a lower maximum PCE of 8.67%, which could be attributed to the weaker near-field electric enhancement of Au NPs compared to Au NSs. Incorporation of Au NSs in a different layer such as the PEDOT:PSS layer was also investigated, and the resulting *J–V* characteristics and photovoltaic parameters are shown in Figure S5 and Table S2. As expected, the maximum PCE of 8.49% was lower than the maximum PCE obtained by embedding Au NSs and Au NPs in the active layer. This could be attributed due to the greater size of the Au NSs (~30 nm) compared to the PEDOT:PSS film thickness (~10 nm), which would provide a direct pathway for electrons to travel from the active layer to the anode, thereby enhancing recombination.

Figure 2b depicts typical *J–V* characteristics of planar PSCs without Au NSs (denoted as control) and with Au NSs embedded in the HTL. Incorporation of Au NSs significantly increased J_{sc} and FF relative to those of the control, whereas V_{oc} remained nearly the same. As a result, PCE was enhanced from 12.49% to 13.97%, as summarized in Table 1, and the relationship between photovoltaic performance and Au NSs concentration is plotted in Figure S3. Placing Au NSs in the $MAPbI_3$ layer degraded the J_{sc} and V_{oc} as well as the FF (Figure S6). This detrimental effect could arise from the presence of Au NS impurities influencing the crystallinity of the $MAPbI_3$ and known to cause nonradiative recombination in PSCs.[33] Overall, the above results suggest that embedding Au NSs into the active layer of OSCs and perovskite/HTL interface of PSCs could improve their PCEs by 6% and 14% under the optimized concentrations of 0.01 and 0.02 wt%, respectively.

To further evaluate the effect of plasmon-enhanced scattering upon J_{sc} improvement in the corresponding wavelength range, the incident photon–to–current efficiency (IPCE) was measured with and without Au NSs. The IPCE spectra shows systematic increases for both OSCs and PSCs when Au NSs were incorporated (Figs. 2c,d), which is consistent with the improvements to J_{sc} listed in Table 1. The IPCE enhancement spectra (ΔIPCE) clearly showed a maximum peak at 510 nm for OSCs; for PSCs the peaks were bathochromically shifted and demonstrated two distinct peaks at 580 and 740 nm, indicating significant enhancement of light absorption by means of incorporating Au NSs. The shifts of ΔIPCE observed for embedding Au NSs in the PSCs were mainly attributed to the higher refractive index of perovskite[34] compared to that of the PTB7:PCBM layer.[35-36] To confirm the above findings, total light absorption was carried out using reflectance measurements for the incident light from the ITO side of real OSC and PSC device structures, as shown in Figures S7a and S7b. The calculated absorption enhancement (Δα) clearly showed peaks similar to those for the ΔIPCE spectra. However, the ΔIPCE spectra demonstrated broadband enhancement over the visible range, suggesting that improvement of IPCE is affected by both optical and electrical properties in OSCs and PSCs.

To verify the improvement of light absorption after incorporation of Au NSs and the underlying contributions of plasmonic optical effects, theoretical simulations were performed using the finite element method. Figure 3 shows the electric field distribution of Au NSs positioned in the PTB7:PCBM and spiro-OMeTAD layers at certain excitation wavelengths (λ_{ex}) according to the peaks observed in the ΔIPCE spectra. The positions of Au NSs in the OSCs and PSCs were simulated based on the cross sections depicted in Figure S2. Note that for perovskite/spiro-OMeTAD, the incoming light direction was simulated from perovskite film. Figure 3a shows the Au NSs in the PTB7:PCBM layer, suggesting that the improvement of light

absorption was partially due to near-field enhancement via the SPR effect. Meanwhile, the electric field around the surface of the particle was much stronger in the perovskite/spiro-OMeTAD interface (Figures 3b,c). The weak electric field intensity of Au NSs in OSCs is known to arise from the higher absorption coefficient of PTB7:PCBM,[28] resulting in suppression of light scattering. Further enhancement in the field at the round edges of Au NS tips was observed when excited at an NIR wavelength (λ_{ex} = 740 nm), leading to field decay that reached the perovskite layer (refer to Figure S8). These results can be attributed to near-field enhancement and the simultaneous backscattering effect, which prolong the optical pathway and provide more photogeneration in the perovskite layer. Based on a previous report,[31] we can deduce that the two distinct peaks observed in the ΔIPCE spectra originated from the SPR effect of Au NSs and light scattering.

To better understand the effects of Au NSs embedded in OSCs and PSCs, we further employed Raman spectroscopy as shown in Figures 4a and b, yielding spectra with peak features of PTB7 and spiro-OMeTAD that were in good agreement with previous reports.[37-38] The Raman intensity of both OSCs and PSCs improved significantly in the cases where Au NSs were incorporated, indicating that plasmonic near-field enhancement by Au NSs could lead to improved light absorption. In addition, charge dissociation or separation in the presence of Au NSs was investigated by means of photoluminescence (PL) measurements of both PTB7 and the perovskite/thin layer of spiro-OMeTAD (dopant-free) films coated on glass substrates with and without Au NSs. The films embedded with Au NSs showed relatively lower PL intensities than pure PTB7 and spiro-OMeTAD (Figures 4c and d), a trend that is in accordance with previous studies[20, 39] and is attributed to the strong local electric field in the vicinity of Au NSs, which promotes efficient charge separation of photogenerated excitons in the active layer of OSCs and

charge transfer at the perovskite/spiro-OMeTAD interface of PSCs. Similarly, time-resolved PL (TRPL) showed slightly shorter exciton lifetimes for PTB7:Au NSs (631 ps) than for pristine PTB7 (641 ps; Figure S9a). Due to the detection limit of TRPL measurements, the exciton lifetime of perovskite/spiro-OMeTAD could not recorded; however, it is expected that the lifetime is shorter when Au NSs are present, owing to increased PL quenching.

The exciton generation rate and charge collection probability of OSCs, denoted respectively as G_{max} and P(E,T), were calculated to investigate improvements in J_{sc}. Photocurrent density is plotted versus effective voltage in Figure S9b and the calculations are explained in the *Supporting Information*. The incorporation of Au NSs yielded the slightly higher calculated G_{max} value of 1.23×10^{28} s^{-1} m^{-3} compared to 1.11×10^{28} s^{-1} m^{-3} for the control device; similarly, P(E,T) under the short circuit condition (refer to Figure S9c) showed a slight increment from 85% to 88% with the incorporation of Au NSs. This revealed that Au NSs in the active layer contributed to both light absorption and charge dissociation, which is in good agreement with the reflectance spectra and PL quenching trend. The higher J_{ph} of OSCs with Au NSs also indicated that Au NSs improved the charge extraction efficiency and led to an enhanced FF,[40] as shown in Table 1. For further analysis, impedance spectroscopy (IS) under illumination was carried out with various applied biases (V_{app}) for both OSCs and PSCs, under constant white LED illumination; the corresponding Nyquist plots are presented in Figure S10. According to the literature,[41-42] the IS responses of OSCs and PSCs are composed of two different arcs in the Nyquist plot: the first arc (high frequency) is mainly attributed to the charge transport resistance at the HTL, denoted R_{HTM}, and the second arc (low frequency) corresponds to the charge recombination resistance, denoted R_{rec}. Subsequently, the equivalent circuit in Figure S10 was used to extract the R_{rec} of OSCs and the R_{HTL} of PSCs, both with and without Au NSs (Figs.

5a,b). It can be clearly seen from Figure 5a that the R_{rec} of OSCs with Au NSs was significantly lower compared to that of the control device, even at high V_{app}. The low R_{rec} indicates that embedding Au NSs enhances the charge carrier density[43] and energy barrier to hole extraction,[44] thereby increasing V_{oc}. Moreover, Figure 5b shows that the R_{HTL} of PSCs with Au NSs was dramatically suppressed compared to that of the control device, indicating that the Au NSs reduced the hole transport resistance and consequently improved the hole collection transport properties of spiro-OMeTAD. These results explained the higher FF observed in the *J–V* measurements.

Figures 5c and d show the results of intensity modulated photovoltage and photocurrent spectroscopies (IMPS and IMVS) carried out under red LED illumination with a wavelength of 635 nm to investigate the charge recombination (τ_R) and transport (τ_{CT}) times of fabricated OSCs and PSCs. OSCs embedded with Au NSs showed better τ_R of 148 μs compared to the 64 μs of the control device, suggesting suppression of recombination, whereas τ_{CT} differed negligibly in the cases with and without Au NSs (Figure S11). These results explained the slight increment of V_{oc} of OSCs observed in the *J–V* measurements. For PSCs, the calculated τ_{CT} values were 15 and 4 μs without and with Au NSs, respectively, where the τ_{CT} values are relatively larger within the given range of current density (as shown in Figure S12), implying a fast hole-transfer rate and efficient hole collection. The faster charge transport within the spiro-OMeTAD may be due to the enhancement in hole mobility provided by the Au NSs, thus explaining the J_{sc} increment listed in Table 1.

Conclusions

We have demonstrated the incorporation of highly dispersed Au NSs within the active layer of OSCs and perovskite/HTL interface (rear contact) of PSCs by means of solution processing. The PCEs of both OSCs and PSCs embedded with Au NSs were significantly improved by 6 and 14%, respectively, due to their enhanced optical and electrical properties. Optically, Au NSs improved light absorption by means of the SPR effect in OSCs, while the improvement for PSCs was due to both SPR and backscattering effects. Electronically, the strong electric field of Au NSs caused efficient charge separation within the active layers of OSCs and enhanced charge transfer at the perovskite/spiro-OMeTAD interface. The electrical improvements are considered to be due to the reduced charge recombination rates and faster charge transport observed in both OSCs and PSCs with the incorporation of Au NSs. The present work provides useful guidelines and new designs to achieve high-performance solar cells and other optoelectronic devices that exploit the effects of dual plasmonic nanostructures.

Acknowledgements

This work was supported by the Pioneer Research Center Program (NRF-2013M3C1A3065528), by the Basic Science Research Program (NRF-2017R1A2B2001838 and NRF-2014R1A4A1008140), and by Creative Materials Discovery Program (NRF-2017M3D1A1039288) through the National Research Foundation (NRF) of Korea, funded by the Ministry of Science, ICT & Future Planning. R.T.G. acknowledges support of this work by the Korea Research Fellowship Program through the NRF of Korea funded by the Ministry of Science, ICT and Future Planning.

Experimental details

Materials. Gold chloride trihydrate ($HAuCl_4 \cdot 3H_2O$; ≥99.99%), mPEG-thiol (mPEG-SH; M.W: 6,000), sodium citrate tribasic dihydrate (≥99%), hydroxylamine hydrochloride (99.99%), and polyvinylpyrrolidone (PVP; M.W. 40,000) were obtained from Sigma-Aldrich (St. Louis, MO, USA). All reagents and chemicals were used without further purification. ZnO sol-gel was prepared by dissolving 1.64 g of zinc acetate dihydrate ($Zn(CH_3COO)_2 \cdot 2H_2O$; Aldrich, 99.9%) and 0.5 g of ethanolamine ($NH_2CH_2CH_2OH$; Aldrich, 99.5%) in 10 g of 2-methoxyethanol ($CH_3OCH_2CH_2OH$; Aldrich, 99.8%), followed by stirring at room temperature for 30 min.[45] PEDOT:PSS Clevios P VP AI 4083 was purchased from Heraeus. Lead iodide (99%), 4-tert-butylpyridine (tBP), and bis(trifluoromethane)sulfonimide lithium salt (LiTFSi) were purchased from Aldrich. Methylammonium iodide (MAI) was purchased from Dyesol, and spiro-OMeTAD was purchased from Lumtec, Taiwan.

Synthesis of mPEG-modified gold nanoparticles and nanostars (mPEG-AuNPs and mPEG-Au NSs). Au NSs were synthesized by means of a two-step seed-mediated growth method.[46] In the first step, colloidal Au NP solution was synthesized by adding 15 mL of 5 mM sodium citrate solution to 100 mL of boiling hot 0.25 mM $HAuCl_4$ under vigorous stirring. The solution was constantly stirred for 15 min after the sodium citrate addition and was then cooled to room temperature. The reaction mixture was centrifuged at 8000 rpm for 15 min to collect the Au NPs, the supernatant was discarded, and the Au NPs were redispersed in distilled water and stored at 4 °C. In the second step, 2 mL of a dispersion of as-synthesized Au NPs (~20 nm) having an optical density of 1 (at λ_{max} = 520 nm) was added to a conical centrifuge tube, and to this 1 mL of 1% PVP and 200 μL of 0.1 M phosphate buffer (pH 8.0) were also added. Then, 400 μL of 0.1

M NH_2OH-HCl solution was added, followed by dropwise addition of 400 μL of 5 mM $HAuCl_4$ under slow vortexing. The solution changed from red to dark blue, indicating the formation of Au NSs. The solution was vortexed for a few seconds and then centrifuged at 8000 rpm for 15 min. To modify the surfaces of the Au NPs or Au NSs with mPEG-SH, 6 mg of mPEG-SH was dissolved in 500 μL of distilled water and then 160 μL of this solution was added to 10 mL of a solution of Au NPs or Au NSs. The mixture was shaken for 1 h and then the particles were collected by means of centrifugation at 8000 rpm for 15 min. Finally, the desired concentration of particles was redispersed in chlorobenzene solution including a small amount of methanol.

Fabrication process of OSC devices. ITO-coated substrates were precleaned by means of ultrasonication in acetone, methanol, and boiling iso-propanol for 10 min each, and then dried in a 120 °C oven for 1 h. Subsequently, the ITO was ultraviolet ozone (UVO)-treated for 15 min and the ZnO sol-gel solution was spin-casted onto the ITO at 5000 rpm for 40 s, followed by dynamic annealing to 150 °C for 20 min in ambient air, yielding a thickness of 20 nm. An active layer with a thickness of 90 nm was deposited on top of the ZnO layer in an N_2-filled glove box from a solution of 8 mg PTB7 and 12 mg PCBM (1:1.5) in chlorobenzene/1,8-diiodooctane (97:3 by volume). Different concentrations of mPEG-Au NSs, namely 0.01, 0.03, and 0.12 wt%, were blended into the PTB7:PCBM solution. Afterwards, PEDOT:PSS was spin casted over the active layer at 5000 rpm for 50 s to form a 10 nm HTL. Without further drying, a 100-nm thickness layer of Ag was deposited by thermal evaporation at ~10^{-6} Torr through a shadow mask with active area of 0.096 cm^2.

Fabrication of PSC devices. A ZnO thin film was coated onto ITO substrates in a manner similar to the above procedures. The method of depositing a 250 nm perovskite layer on top of the ZnO layer can be found in our previous work.[47] An HTL was deposited by means of spin

coating a spiro-OMeTAD solution doped with Li-TFSI and tBP over the perovskite film at 3000 rpm for 60 s; to incorporate Au NSs into the HTL, various concentrations of mPEG-Au NSs (i.e. 0.01, 0.02, and 0.03 wt%) were blended into the spiro-OMeTAD solution. Finally, a 100-nm layer of Ag was deposited on top of the HTL via thermal evaporation at ~10^{-6} Torr through a metal mask with active area 0.096 cm^2.

Materials and Device Characterization. Cross-sectional FESEM images of OSC and PSC devices were acquired using a Hitachi S-4800 FESEM instrument, and high-resolution TEM (HRTEM) images of Au NSs were acquired using a Zeiss EM-912 Omega instrument. *J–V* curves were acquired using a Keithley 2400 SMU instrument under simulated AM 1.5G illumination of irradiance 100 mW cm^{-2} (Oriel Sol 1A, Newport). IPCE spectra of OSCs and PSCs were acquired using a quantum efficiency measurement instrument (Oriel IQE-200) consisting of a 250 W quartz tungsten halogen lamp as the light source, a monochromator, an optical chopper, a lock-in amplifier, and a calibrated silicon photodetector. Reflectance spectra of OSCs and PSCs were acquired using a Perkin Elmer 950 UV/Vis/NIR spectrophotometer. Raman shifts of PTB7 and spiro-OMeTAD were characterized by means of Raman spectroscopy (Nanofinder 30, Tokyo Instruments Inc.), using laser excitation with a 488 nm wavelength and 1 mW power; PL measurements were carried out using a Jasco FP-6500 spectrofluorometer with an excitation wavelength of 580 nm for PTB7 and 650 nm for perovskite/spiro-OMeTAD. To obtain TRPL spectra, PTB7 thin films with and without Au NSs were excited at 532 nm and exciton dynamics were recorded using a time-correlated single photon counting (TCSPC) spectrometer (FLS920-T, Edinburgh Instruments). Impedance spectroscopy, IMVS, and IMPS were carried out using an impedance analyzer (CompactStat, IVIUM Tech.) equipped with an LED module; Nyquist plots were fitted using the ZView software (Scribner Associates).

Theoretical simulation. All calculated optical spectra and electric field distribution profiles were calculated by means of the finite element method using the ANSYS HFSS software (ANSYS, Inc., USA). A 35 nm Au NS was simulated as a 20 nm Au nanoparticle with 7.5 nm long round-edge branches from the core to resemble a star shape. The positions of Au NSs in the center of PTB7:PCBM for OSCs and in spiro-OMeTAD layer where only 10 nm above the boundary of perovskite layer based on the cross section in Figure S1. The dimension of whole layers was the same as for the schematic view and plane waves propagated along the Z direction with polarization along the X direction. The simulation region, including the radiation box for boundary conditions, was $1\times1\times1$ μm^3, with a minimum mesh volume of 0.08 nm^3.

Supporting Information

Gold nanostars (Au NSs) size distribution, position of Au NSs photovoltaic performance of organic and perovskite solar cells, reflectance analysis, optical simulation, time-resolved photoluminescence, photocurrent generation, and Nyquist plot.

References

(1) Zhao, W.; Li, S.; Yao, H.; Zhang, S.; Zhang, Y.; Yang, B.; Hou, J. Molecular Optimization Enables over 13% Efficiency in Organic Solar Cells. *J. Am. Chem. Soc.* **2017,** *139* (21), 7148–7151.

(2) Shin, S. S.; Yeom, E. J.; Yang, W. S.; Hur, S.; Kim, M. G.; Im, J.; Seo, J.; Noh, J. H.; Seok, S. I. Colloidally Prepared La-doped BaSnO3 Electrodes for Efficient, Photostable Perovskite Solar Cells. *Science* **2017,** *356* (6334), 167-171.

(3) Tavakoli, M. M.; Tsui, K.-H.; Zhang, Q.; He, J.; Yao, Y.; Li, D.; Fan, Z. Highly Efficient Flexible Perovskite Solar Cells with Antireflection and Self-Cleaning Nanostructures. *ACS Nano* **2015,** *9* (10), 10287-10295.

(4) Chen, Y.; Elshobaki, M.; Gebhardt, R.; Bergeson, S.; Noack, M.; Park, J.-M.; Hillier, A. C.; Ho, K.-M.; Biswas, R.; Chaudhary, S. Reducing Optical Losses in Organic Solar Cells using Microlens Arrays: Theoretical and Experimental Investigation of Microlens Dimensions. *Phys. Chem. Chem. Phys.* **2015,** *17* (5), 3723-3730.

(5) Li, X.; Choy, W. C.; Huo, L.; Xie, F.; Sha, W. E.; Ding, B.; Guo, X.; Li, Y.; Hou, J.; You, J. Dual Plasmonic Nanostructures for High Performance Inverted Organic Solar Cells. *Adv. Mater.* **2012,** *24* (22), 3046-3052.

(6) Guldin, S.; Hüttner, S.; Kolle, M.; Welland, M. E.; Müller-Buschbaum, P.; Friend, R. H.; Steiner, U.; Tétreault, N. Dye-Sensitized Solar Cell Based on a Three-Dimensional Photonic Crystal. *Nano Letters* **2010,** *10* (7), 2303-2309.

(7) Meng, K.; Gao, S.; Wu, L.; Wang, G.; Liu, X.; Chen, G.; Liu, Z.; Chen, G. Two-Dimensional Organic–Inorganic Hybrid Perovskite Photonic Films. *Nano Lett.* **2016,** *16* (7), 4166-4173.

(8) Jang, Y. H.; Jang, Y. J.; Kim, S.; Quan, L. N.; Chung, K.; Kim, D. H. Plasmonic Solar Cells: From Rational Design to Mechanism Overview. *Chem. Rev.* **2016,** *116* (24), 14982-15304.

(9) Chan, K.; Wright, M.; Elumalai, N.; Uddin, A.; Pillai, S. Plasmonics in Organic and Perovskite Solar Cells: Optical and Electrical Effects. *Adv. Opt. Mater.* **2016,** *5*, 1600698.

(10) Garcia, M. A. Surface Plasmons in Metallic Nanoparticles: Fundamentals and Applications. *J. Phys. D: Appl. Phys.* **2011,** *44* (28), 283001.

(11) Schwartzkopf, M.; Santoro, G.; Brett, C. J.; Rothkirch, A.; Polonskyi, O.; Hinz, A.; Metwalli, E.; Yao, Y.; Strunskus, T.; Faupel, F.; Müller-Buschbaum, P.; Roth, S. V. Real-Time Monitoring of Morphology and Optical Properties during Sputter Deposition for Tailoring Metal–Polymer Interfaces. *ACS Appl. Mater. Interfaces* **2015,** *7* (24), 13547-13556.

(12) Park, H. I.; Lee, S.; Lee, J. M.; Nam, S. A.; Jeon, T.; Han, S. W.; Kim, S. O. High Performance Organic Photovoltaics with Plasmonic-Coupled Metal Nanoparticle Clusters. *ACS Nano* **2014,** *8* (10), 10305-10312.

(13) Wu, J.-L.; Chen, F.-C.; Hsiao, Y.-S.; Chien, F.-C.; Chen, P.; Kuo, C.-H.; Huang, M. H.; Hsu, C.-S. Surface Plasmonic Effects of Metallic Nanoparticles on the Performance of Polymer Bulk Heterojunction Solar Cells. *ACS Nano* **2011,** *5* (2), 959-967.

(14) Baek, S.-W.; Noh, J.; Lee, C.-H.; Kim, B.; Seo, M.-K.; Lee, J.-Y. Plasmonic Forward Scattering Effect in Organic Solar Cells: A Powerful Optical Engineering Method. *Sci. Rep.* **2013,** *3*, 1726.

(15) Janković, V.; Yang, Y.; You, J.; Dou, L.; Liu, Y.; Cheung, P.; Chang, J. P.; Yang, Y. Active Layer-Incorporated, Spectrally Tuned Au/SiO2 Core/Shell Nanorod-Based Light Trapping for Organic Photovoltaics. *ACS Nano* **2013,** *7* (5), 3815-3822.

(16) Baek, S.-W.; Park, G.; Noh, J.; Cho, C.; Lee, C.-H.; Seo, M.-K.; Song, H.; Lee, J.-Y. Au@Ag Core–Shell Nanocubes for Efficient Plasmonic Light Scattering Effect in Low Bandgap Organic Solar Cells. *ACS Nano* **2014,** *8* (4), 3302-3312.

(17) Lu, L.; Luo, Z.; Xu, T.; Yu, L. Cooperative Plasmonic Effect of Ag and Au Nanoparticles on Enhancing Performance of Polymer Solar Cells. *Nano Lett.* **2013,** *13* (1), 59-64.

(18) Choi, H.; Lee, J.-P.; Ko, S.-J.; Jung, J.-W.; Park, H.; Yoo, S.; Park, O.; Jeong, J.-R.; Park, S.; Kim, J. Y. Multipositional Silica-Coated Silver Nanoparticles for High-Performance Polymer Solar Cells. *Nano Lett.* **2013,** *13* (5), 2204-2208.

(19) Heo, M.; Cho, H.; Jung, J.-W.; Jeong, J.-R.; Park, S.; Kim, J. Y. High-Performance Organic Optoelectronic Devices Enhanced by Surface Plasmon Resonance. *Advanced Materials* **2011,** *23* (47), 5689-5693.

(20) Zhang, W.; Saliba, M.; Stranks, S. D.; Sun, Y.; Shi, X.; Wiesner, U.; Snaith, H. J. Enhancement of perovskite-based solar cells employing core–shell metal nanoparticles. *Nano Lett.* **2013,** *13* (9), 4505-4510.

(21) Saliba, M.; Zhang, W.; Burlakov, V. M.; Stranks, S. D.; Sun, Y.; Ball, J. M.; Johnston, M. B.; Goriely, A.; Wiesner, U.; Snaith, H. J. Plasmonic□Induced Photon Recycling in Metal Halide Perovskite Solar Cells. *Adv. Funct. Mater.* **2015,** *25* (31), 5038-5046.

(22) Ye, T.; Ma, S.; Jiang, X.; Wei, L.; Vijila, C.; Ramakrishna, S. Performance Enhancement of Tri□Cation and Dual□Anion Mixed Perovskite Solar Cells by Au@ SiO2 Nanoparticles. *Adv. Funct. Mater.* **2017**, 1606545.

(23) Cui, J.; Chen, C.; Han, J.; Cao, K.; Zhang, W.; Shen, Y.; Wang, M. Surface Plasmon Resonance Effect in Inverted Perovskite Solar Cells. *Adv. Sci.* **2016,** *3*, 1500312.

(24) Wu, R.; Yang, B.; Zhang, C.; Huang, Y.; Cui, Y.; Liu, P.; Zhou, C.; Hao, Y.; Gao, Y.; Yang, J. Prominent Efficiency Enhancement in Perovskite Solar Cells Employing Silica-Coated Gold Nanorods. *J. Phys. Chem. C* **2016,** *120* (13), 6996-7004.

(25) Zhang, G.; Hawks, S. A.; Ngo, C.; Schelhas, L. T.; Scholes, D. T.; Kang, H.; Aguirre, J. C.; Tolbert, S. H.; Schwartz, B. J. Extensive Penetration of Evaporated Electrode Metals into Fullerene Films: Intercalated Metal Nanostructures and Influence on Device Architecture. *ACS Appl. Mater. Inter.* **2015,** *7* (45), 25247-25258.

(26) Wang, J.-Y.; Hsu, F.-C.; Huang, J.-Y.; Wang, L.; Chen, Y.-F. Bifunctional Polymer Nanocomposites as Hole-Transport Layers for Efficient Light Harvesting: Application to Perovskite Solar Cells. *ACS Appl. Mater. Interfaces* **2015,** *7* (50), 27676-27684.

(27) Lee, D. S.; Kim, W.; Cha, B. G.; Kwon, J.; Kim, S. J.; Kim, M.; Kim, J.; Wang, D. H.; Park, J. H. Self-Position of Au NPs in Perovskite Solar Cells: Optical and Electrical Contribution. *ACS Appl. Mater. Interfaces* **2015,** *8* (1), 449-454.

(28) Kakavelakis, G.; Vangelidis, I.; Heuer□Jungemann, A.; Kanaras, A. G.; Lidorikis, E.; Stratakis, E.; Kymakis, E. Plasmonic Backscattering Effect in High□Efficient Organic Photovoltaic Devices. *Adv. Energy Mater.* **2016,** *6* (2), 1501640.

(29) Kozanoglu, D.; Apaydin, D. H.; Cirpan, A.; Esenturk, E. N. Power Conversion Efficiency Enhancement of Organic Solar Cells by Addition of Gold Nanostars, Nanorods, and Nanospheres. *Org. Electron.* **2013,** *14* (7), 1720-1727.

(30) Niu, W.; Chua, Y. A. A.; Zhang, W.; Huang, H.; Lu, X. Highly Symmetric Gold Nanostars: Crystallographic Control and Surface-Enhanced Raman Scattering Property. *J. Am. Chem. Soc.* **2015,** *137* (33), 10460-10463.

(31) Ren, X.; Cheng, J.; Zhang, S.; Li, X.; Rao, T.; Huo, L.; Hou, J.; Choy, W. C. High Efficiency Organic Solar Cells Achieved by the Simultaneous Plasmon□Optical and Plasmon□Electrical Effects from Plasmonic Asymmetric Modes of Gold Nanostars. *Small* **2016,** *12* (37), 5200-5207.

(32) Chen, H.; Kou, X.; Yang, Z.; Ni, W.; Wang, J. Shape- and Size-Dependent Refractive Index Sensitivity of Gold Nanoparticles. *Langmuir* **2008,** *24* (10), 5233-5237.

(33) Domanski, K.; Correa-Baena, J.-P.; Mine, N.; Nazeeruddin, M. K.; Abate, A.; Saliba, M.; Tress, W.; Hagfeldt, A.; Grätzel, M. Not All that Glitters is Gold: Metal-Migration-Induced Degradation in Perovskite Solar Cells. *ACS Nano* **2016,** *10* (6), 6306-6314.

(34) Löper, P.; Stuckelberger, M.; Niesen, B.; Werner, J.; Filipic, M.; Moon, S.-J.; Yum, J.-H.; Topič, M.; De Wolf, S.; Ballif, C. Complex Refractive Index Spectra of CH3NH3PbI3 Perovskite Thin Films Determined by Spectroscopic Ellipsometry and Spectrophotometry. *J. Phys. Chem. Lett.* **2014,** *6* (1), 66-71.

(35) Hedley, G. J.; Ward, A. J.; Alekseev, A.; Howells, C. T.; Martins, E. R.; Serrano, L. A.; Cooke, G.; Ruseckas, A.; Samuel, I. D. Determining the Optimum Morphology in High-Performance Polymer-Fullerene Organic Photovoltaic Cells. *Nat. Comm.* **2013,** *4*, 2867.

(36) Li, X.; Ren, X.; Xie, F.; Zhang, Y.; Xu, T.; Wei, B.; Choy, W. C. High□Performance Organic Solar Cells with Broadband Absorption Enhancement and Reliable Reproducibility Enabled by Collective Plasmonic Effects. *Advanced Optical Materials* **2015,** *3* (9), 1220-1231.

(37) Razzell-Hollis, J.; Wade, J.; Tsoi, W. C.; Soon, Y.; Durrant, J.; Kim, J.-S. Photochemical Stability of High Efficiency PTB7:PC70 BM Solar Cell Blends. *J. Mater. Chem. A* **2014,** *2* (47), 20189-20195.

(38) Hooper, K.; Lee, H.; Newman, M.; Meroni, S.; Baker, J.; Watson, T.; Tsoi, W. Probing the Degradation and Homogeneity of Embedded Perovskite Semiconducting Layers in Photovoltaic Devices by Raman Spectroscopy. *Phys. Chem. Chem. Phys.* **2017,** *19* (7), 5246-5253.

(39) Beliatis, M. J.; Henley, S. J.; Han, S.; Gandhi, K.; Adikaari, A.; Stratakis, E.; Kymakis, E.; Silva, S. R. P. Organic Solar Cells with Plasmonic Layers Formed by Laser Nanofabrication. *Phys. Chem. Chem. Phys.* **2013,** *15* (21), 8237-8244.

(40) Chen, J. D.; Cui, C.; Li, Y. Q.; Zhou, L.; Ou, Q. D.; Li, C.; Li, Y.; Tang, J. X. Single□ Junction Polymer Solar Cells Exceeding 10% Power Conversion Efficiency. *Adv. Mater.* **2015,** *27* (6), 1035-1041.

(41) Fabregat-Santiago, F.; Garcia-Belmonte, G.; Mora-Seró, I.; Bisquert, J. Characterization of Nanostructured Hybrid and Organic Solar Cells by Impedance Spectroscopy. *Phys. Chem. Chem. Phys.* **2011,** *13* (20), 9083-9118.

(42) Gonzalez-Pedro, V.; Juarez-Perez, E. J.; Arsyad, W.-S.; Barea, E. M.; Fabregat-Santiago, F.; Mora-Sero, I.; Bisquert, J. General Working Principles of CH3NH3PbX3 Perovskite Solar Cells. *Nano Lett.* **2014,** *14* (2), 888-893.

(43) Lu, L.; Luo, Z.; Xu, T.; Yu, L. Cooperative Plasmonic Effect of Ag and Au Nanoparticles on Enhancing Performance of Polymer Solar Cells. *Nano Lett.* **2012,** *13* (1), 59-64.

(44) He, Y.; Liu, C.; Li, J.; Zhang, X.; Li, Z.; Shen, L.; Guo, W.; Ruan, S. Improved Power Conversion Efficiency of Inverted Organic Solar Cells by Incorporating Au Nanorods into Active Layer. *ACS Appl. Mater. Inter.* **2015,** *7* (29), 15848-15854.

(45) Ginting, R. T.; Jung, E.-S.; Jeon, M.-K.; Jin, W.-Y.; Song, M.; Kang, J.-W. Low-Temperature Operation of Perovskite Solar Cells: With Efficiency Improvement and Hysteresis-Less. *Nano Energy* **2016,** *27*, 569-576.

(46) Lee, H.; Nam, S. H.; Jung, Y. J.; Park, S.; Kim, J.-M.; Suh, Y. D.; Lim, D.-K. DNA-Mediated Control of Au Shell Nanostructure and Controlled Intra-Nanogap for a Highly Sensitive and Broad Plasmonic Response Range. *J. Mater. Chem. C* **2015,** *3* (41), 10728-10733.

(47) Ginting, R. T.; Jeon, M.-K.; Lee, K.-J.; Jin, W.-Y.; Kim, T.-W.; Kang, J.-W. Degradation Mechanism of Planar-Perovskite Solar Cells: Correlating Evolution of Iodine Distribution and Photocurrent Hysteresis. *J. Mater. Chem. A* **2017,** *5* (9), 4527-4534.

Table 1. Summary of photovoltaic parameters in PSCs with Au NSs embedded in the active layer and HTL, under AM1.5G illumination of 100 mW cm^{-2}.

Type	Position of Au NSs	V_{oc} (V)	J_{sc} (mA/cm^2)	FF (%)	PCE (%)	PCE_{max} (%)
OSCs	Control	0.747 ± 0.002	15.94 ± 0.28	68.58 ± 1.01	8.17 ± 0.13	8.30
	Active layer	0.752 ± 0.002	16.29 ± 0.10	71.28 ± 0.06	8.72 ± 0.06	8.78
PSCs	Control	1.021 ± 0.013	17.43 ± 0.35	67.32 ± 2.34	11.98 ± 0.51	12.49
	HTL	1.041 ± 0.012	18.21 ± 0.44	72.13 ± 0.46	13.66 ± 0.31	13.97

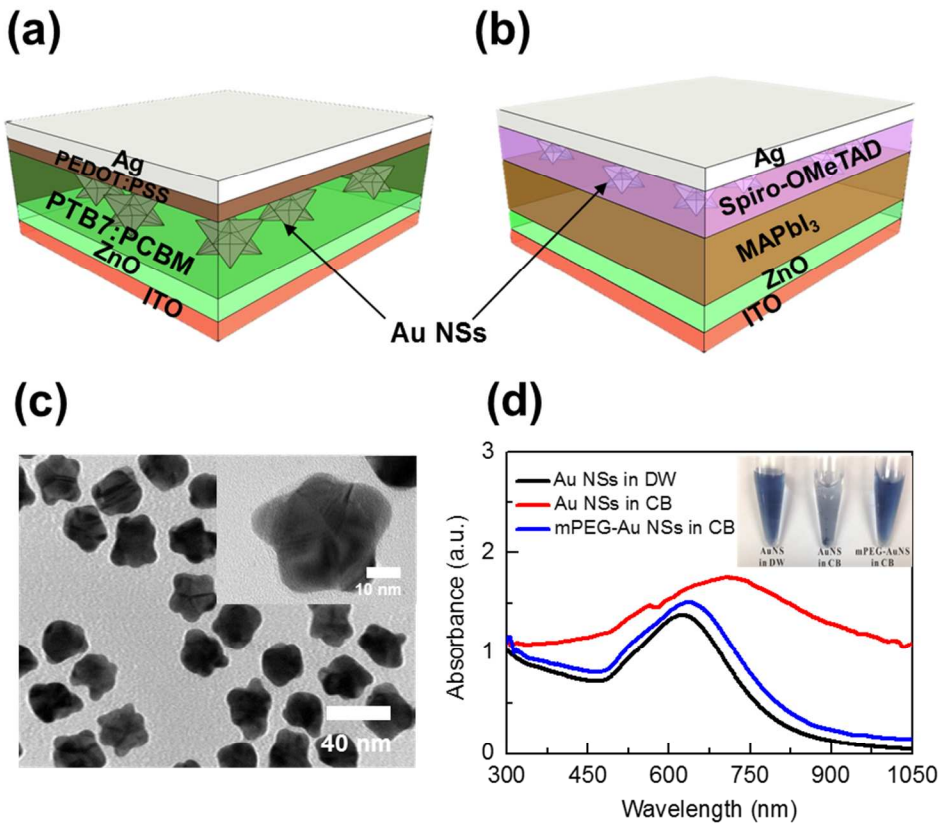

Figure 1. Typical device configurations showing the positions of Au NSs in (a) inverted OSCs and (b) planar-based PSCs. (c) TEM image of Au NSs dispersion in CB solution; (c inset) magnified image of single Au NSs. (d) Optical absorption spectra of Au NSs with and without mPEG-SH modification; (d, inset) dispersions of Au NSs with and without mPEG.

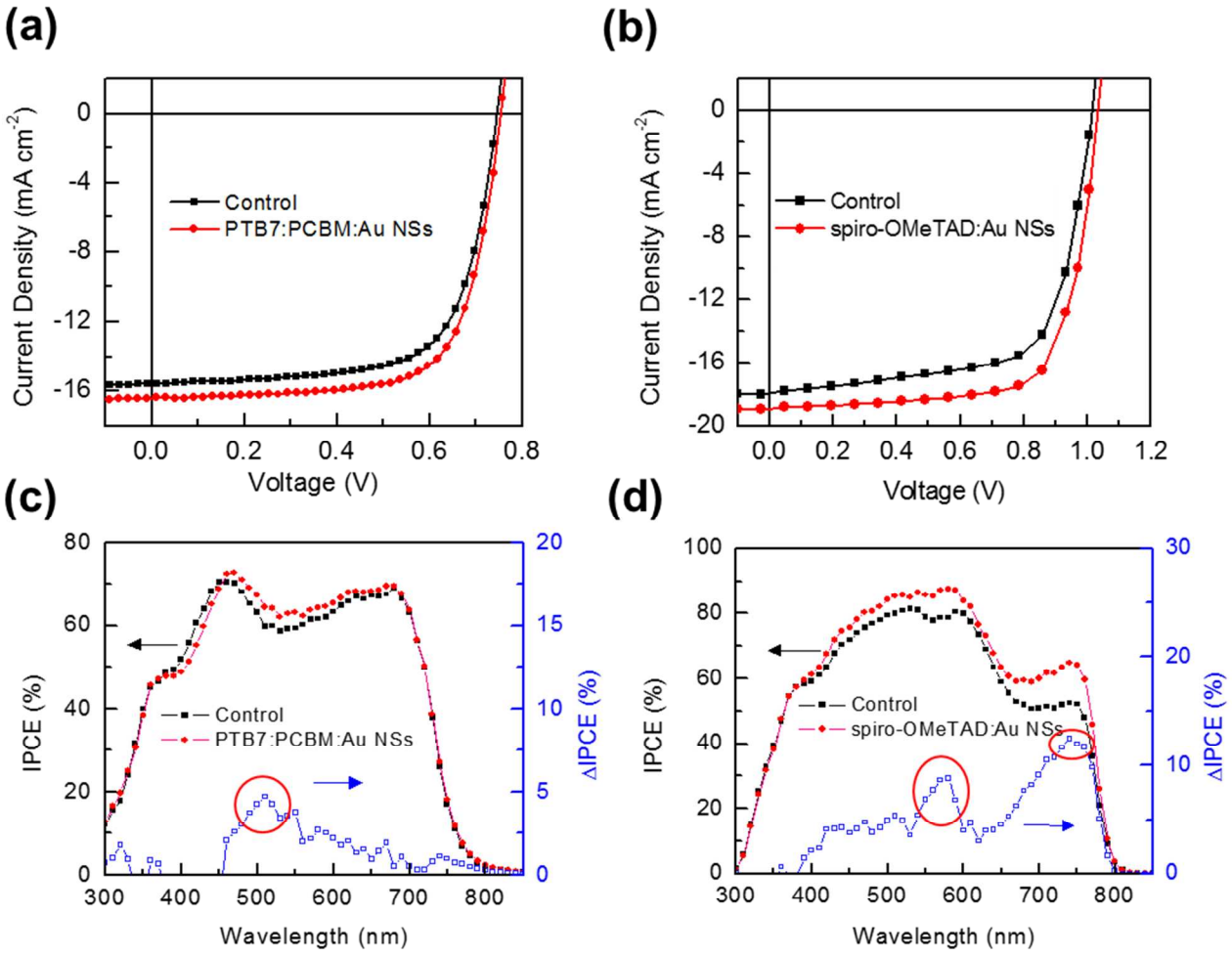

Figure 2. *J–V* characteristics of (a) OSCs and (b) PSCs under AM1.5G illumination of 100 mW cm^{-2}, without and with incorporation of Au NSs. IPCE spectra of (c) OSCs and (d) PSCs; the increase in IPCE is denoted ΔIPCE.

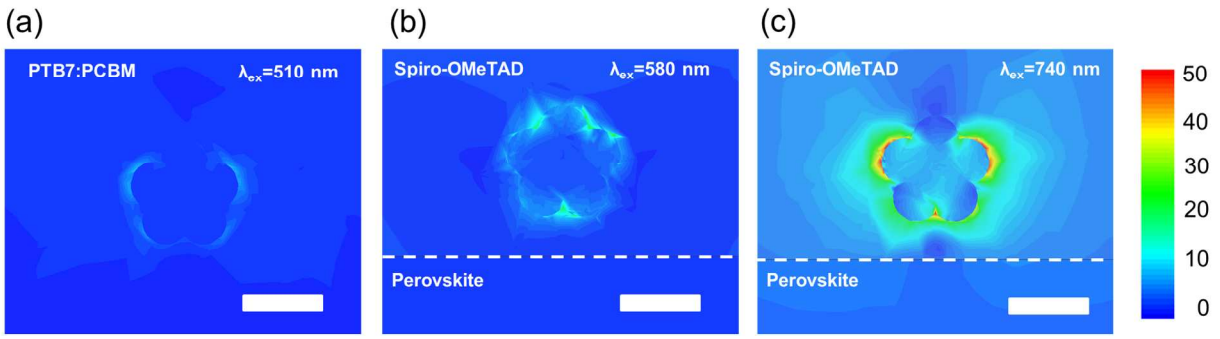

Figure 3. Simulated local electric field distribution around 35 nm Au NSs with respect to the incident light electric field in (a) PTB7:PCBM and (b and c) spiro-OMeTAD. Scale bars: 25 nm; color intensity is expressed as $|E|^2$.

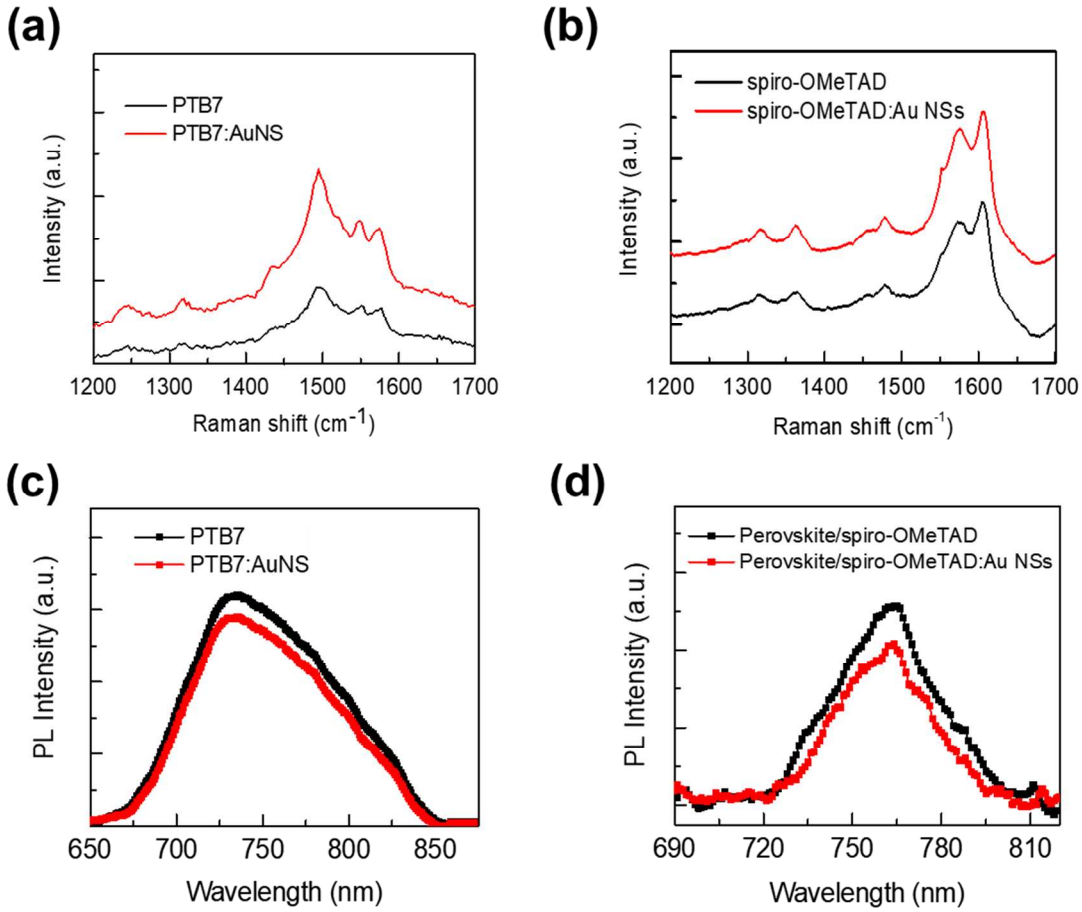

Figure 4. Raman spectra of (a) OSCs and (b) PSCs with and without Au NSs, with an excitation wavelength of 488 nm and a laser power of 1 mW. PL spectra of (c) PTB7 (λ_{ex} = 580 nm) and (d) perovskite/spiro-OMeTAD (λ_{ex} = 650 nm) with and without Au NSs.

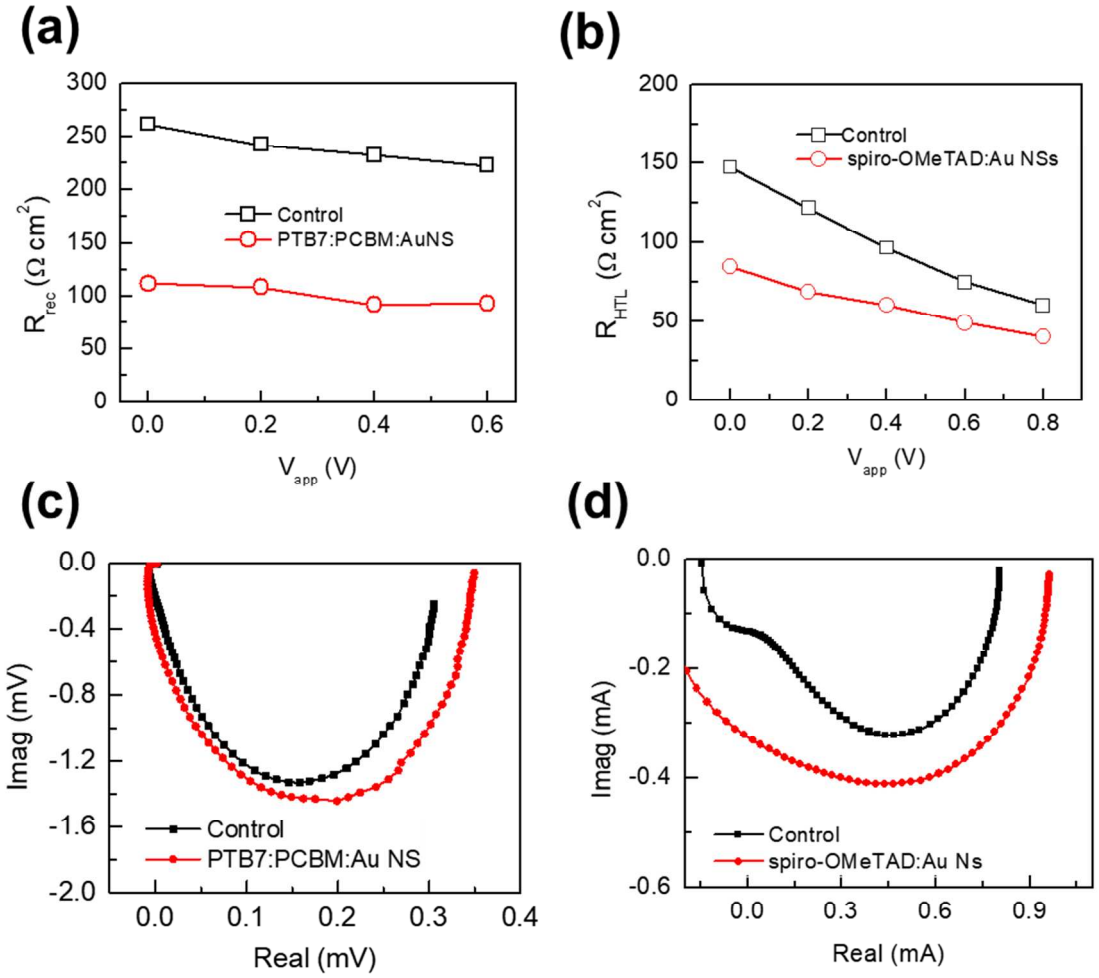

Figure 5. Extracted (a) R_{rec} values of OSCs and (b) R_{HTL} values of PSCs versus applied voltage (V_{app}) under white LED illumination with and without Au NSs. Typical Nyquist plots prepared from (c) IMVS and (d) IMPS spectra of OSCs and PSCs acquired under red LED illumination (635 nm).

Table of content (TOC)